ELSEVIER

Contents lists available at ScienceDirect

Additive Manufacturing

journal homepage: www.elsevier.com/locate/addma



Crystal plasticity approach for predicting mechanical responses in wire-arc directed energy deposition of NbZr1 refractory alloy

Saiful Islam^a, Sainand Jadhav^a, Taejoon Park^{b,*}, Farhang Pourboghrat^{b,c}, Xuesong Fan^d, Peter K. Liaw^d, Duck Bong Kim^{e,*}

- ^a Department of Mechanical Engineering, Tennessee Technological University, Cookeville, TN 38505, United States
- ^b Department of Integrated Systems Engineering, The Ohio State University, Columbus, OH 43210, United States
- ^c Department of Mechanical and Aerospace Engineering, The Ohio State University, Columbus, OH 43210, United States
- d Department of Materials Science and Engineering, The University of Tennessee, Knoxville, TN 37996, United States
- ^e Department of Manufacturing and Engineering Technology, Tennessee Technological University, Cookeville, TN 38505, United States

ARTICLE INFO

Keywords:

Wire-arc directed energy deposition (DED) Refractory alloy Mechanical properties Representative volume element (RVE) Crystal plasticity

ABSTRACT

The refractory alloy, such as Niobium-1 wt% Zirconium (NbZr1) alloy, is a promising candidate for diverse applications in extreme environments. This study investigates an integrated experimental and computational methodology that can predict the mechanical properties of wire-arc directed energy deposited (DED) refractory NbZr1 alloy. The effect of large columnar grains with strong texture induced by the wire-DED process has been successfully incorporated into the representative volume element (RVE). Performing crystal plasticity (CP) simulation on RVE of NbZr1, deformation behavior and stress-strain relationship are predicted to explore the process-structure-property (PSP) relationship. The RVE has been created in synthetic microstructure generation software utilizing the grain statistics derived from electron backscatter diffraction (EBSD) analysis, capturing essential microstructural features. A phenomenological constitutive model and appropriate boundary conditions have been applied and solved, using the CP fast Fourier transform method. The CP model has been calibrated and validated utilizing the tensile test data along the build direction and deposition direction, respectively. The error in predicting yield strength and ultimate tensile strength is 0.91% and 0.67%, respectively, for the calibration simulation, whereas these values are 2.51% and 1.81% for the validation simulation. The results suggest strong agreement between the simulation and experimental observation. Even though global deformation behavior remains consistent across multiple RVEs with the same microstructural features, local stress-strain values vary, indicating structural anisotropy, which is also consistent with the digital image correlation (DIC) result. It is proven that this proposed CP method can effectively predict the mechanical responses of components with large grains and strong textures resulting from the wire-arc DED.

1. Introduction

Refractory metals, such as tungsten (W), niobium (Nb), tantalum (Ta), molybdenum (Mo), and rhenium (Re), and their alloys, exhibit extraordinary melting points surpassing 2400 °C [1]. These materials possess unique physicochemical attributes, encompassing strengths at high temperature, exceptional thermal conductivities, and resistance to corrosion [2]. These characteristics make them well-suited for ultra-high temperature applications across different industries, such as nuclear, power, chemical, and aerospace [3]. Nevertheless, the application of refractory alloys is mainly limited due to challenges associated with

poor manufacturability and high machining costs [1]. Additive manufacturing (AM) could facilitate new opportunities for fabricating components from refractory alloys with the advantages of near-net shape deposition, resulting in a lower buy-to-fly ratio that reduces material wastage. In addition, it provides the capability for complex geometry fabrication and reduces the need for assembly operation, further enhancing the versatility [4,5].

By utilizing metal AM processes, several research groups have deposited refractory metals and alloys. Deposited W and Mo pure metals and their alloys show inferior mechanical properties due to the presence of defects [6]. Different post-processing including heat treatment, hot

E-mail addresses: 2417@osu.edu (T. Park), dkim@tntech.edu (D.B. Kim).

^{*} Corresponding authors.

isostatic pressure is required to improve their mechanical property which is associated with time and cost. Among refractory metals, pure Nb is the least dense, with a density of 8.57 g/cm³, and shows excellent room temperature ductility (up to 40%) [7]. Notably, Nb-based alloys can retain their strength even at temperatures as high as 1400 °C, exceeding the operational limit for most of the nickel-based superalloys [8,9]. The body-centered-cubic (BCC) crystal structure of Nb provides favorable solubility for alloving elements. The inclusion of Zirconium (Zr) enhances solid-solution strengthening, resulting in improved strength [10]. Specifically, the Nb-1 wt% Zr alloy (NbZr1) demonstrates better ductility, exceptional resistance to irradiation, and considerable strength at elevated temperatures, making it promising for applications as structural components in various industries [11]. The mechanical properties of AM-fabricated Nb-based alloys especially NbZr1 are either better or equivalent compared to conventional methods [1,7]. However, it is noteworthy to mention that the powder bed fusion process is associated with a lack of fusion defects, which degrades part integrity

In this regard, wire-arc directed energy deposition (DED) also known as wire-arc additive manufacturing (WAAM) offers a viable option with the benefits of higher deposition rates (160 g/min.), energy efficiency, and low equipment cost [12]. Furthermore, it can reduce post-machining time by around 15-20%, relative to subtractive manufacturing [13]. Bypass wire-arc DED, a modified WAAM method, can further increase the deposition rate and reduce the heat input to the deposited layers [14]. Islam et al. [7] deposited NbZr1 using tungsten inert gas (TIG)-based WAAM process without porosity and cracks. Although maximum tensile of 418 MPa with an elongation limit of 25% was achieved, the structure exhibited anisotropic characteristics. This phenomenon is caused by the unique microstructure associated with the WAAM process due to the non-equilibrium thermal cycles. A comprehensive understanding of microstructural characteristics, related process parameters, and associated mechanical properties is necessary for part qualification. It requires substantial time and resources to conduct experiments with refractory alloys due to their high cost. For this, computational modeling and simulation analysis can complement experimental analysis by reducing the number of experiments required.

Establishing process-structure-property (PSP) relationships in AM for refractory alloys is crucial for identifying optimal process parameters which can ensure the desired location-specific properties in the fabricated components [4,15]. Nevertheless, it is significantly challenging to develop PSP relationships using experiments alone due to its large dimensionality in the AM design space. Moreover, refractory alloys including NbZr1 are expensive, which inhibits the development of design rules solely focusing on the experimentation due to the resource constraints. In order to address these issues, computational approaches are required for simulating mechanical behavior, thereby accelerating the design rule establishment [15]. However, there is currently a lack of integrated methodology that combines experiment and simulation for establishing the design rules in refractory alloys.

Crystal plasticity (CP) simulations provide a significant advantage in characterizing the deformation behavior of polycrystalline materials due to their unique capability to predict grain-scale stresses and strain fields [16,17]. In addition, these simulations can calculate the crystallographic orientation-dependent lattice strain. During the simulation, the constitutive model incorporates multiple factors, such as the activation of slip systems, microstructural features encompassing grain orientation and morphology, as well as elastic constants and hardening parameters. It facilitates the accurate prediction of mechanical responses in materials comprising heterogeneous microstructures. The CP models are classified as a crystal plasticity finite element method (CPFEM) or crystal plasticity fast Fourier transform (CPFFT) models based on the solvers used to solve the boundary-value problems [18]. Both models can capture the detailed complexity of the plastic deformation at the mesoscale and provide a better prediction of the realistic deformation process, as compared to traditional FEM. Nevertheless,

CPFFT models are computationally more efficient since they do not need to calculate the global stiffness matrix, a requirement in CPFEM models [18].

Researchers have applied the CP model to predict the mechanical and anisotropic characteristics of numerous polycrystalline materials including Mg alloy [19], copper [20,21], aluminum [22], and steel [23, 24]. CPFEM has also been applied to study the mechanical deformation under the tensile tests of refractory metals. Lim et al. [25] applied integrated experimental and CPFEM to investigate the deformation of columnar tantalum (Ta) oligo-crystals. An interrupted tensile test at different strain levels was conducted and surface level strain was measured using the high-resolution digital image correlation (DIC) data. The simulation result showed good agreement with the experiments. In another study, geometrically necessary dislocations and their effect on back stress were experimentally and computationally quantified in Ta samples. The results indicated that back stress contributed to 25% of the overall flow stress in the CPFEM simulation [26]. Wang et al. [27] investigated the deformation characteristics of irradiated tungsten (W) under uniaxial compression test at elevated service temperatures utilizing a mechanism-based CPFEM approach. The model accounted for various attributes such as thermal softening and irradiation hardening. The precited macroscopic stress-strain results matched closely to the experimental results. In a study by Xiao et al. [28], CPFEM was utilized to simulate loading curves under nano-indentation for pure W at elevated temperatures. Numerous plasticity parameters were also calculated including lattice friction and dislocation grain interaction for varied temperature ranges (300-600 K). In the study of Ahn et al. [29], grain texture and morphology effects on yield anisotropy were investigated by employing a grain-shape model combined with CPFEM for Zr-2.5 wt% Nb alloy pressure tube. The results indicated that texture had more significant effect on anisotropy compared to grain morphology.

Computational modeling is being used to study the mechanical responses of AM components. In the study of Zhang et al. [17], CPFFT simulations were performed to evaluate the impact of Al-phase hardening parameters and different microstructural features on the mechanical properties of additively manufactured AlSi10Mg alloy. CP model parameters were calibrated using experimental results from in-situ x-ray diffraction. Azhari et al. [30] established the multiscale FFT method for the Ti-6Al-4 V, fabricated using the selective laser melting process to predict stress-strain curves up to fracture. Crack band theory was incorporated with the CP model to accomplish this behavior. In the study of Chakrabarty et al. [31], through a combination of experiments and CPFEM simulations, the impact of grain morphologies on the tensile performance of additively fabricated AlSi10Mg alloy was elucidated. CP constitutive parameters were calibrated by developing an interactive ABAQUS and MATLAB environment utilizing genetic algorithm code. Motaman et al. [32] used physics-based CP constitutive modeling to investigate the effect of plastic anisotropy due to the presence of heterogeneous microstructures in laser powder bed fusion (LPBF) manufactured HMnS. The study also found that grain morphology and texture had equal effect on the stress-strain curve. In Acar et al. [33], columnar grains and crystal orientations in AM alloys were incorporated in CPFEM simulations. Through Voronoi tessellation, multiple microstructures were generated, and the load was applied to mimic the condition of the uniaxial tensile test in three different orientations. Flow stress varies significantly due to varied loading directions. It is evident that CP models can successfully predict the mechanical behavior of AM components.

Existing literature reveals that the CP model has been individually applied to study the mechanical behavior of refractory alloys and AM-fabricated components. However, the CPFFT method, specifically for predicting the stress-strain relationship in refractory NbZr1 alloy fabricated by the WAAM process, has not been investigated. Unique microstructural characteristics observed in WAAM NbZr1 [7], such as large columnar grains with strong texture along build direction, are challenging to incorporate in the RVEs. Consequently, this study aims to

address these research gaps and overcome technical challenges by presenting an integrated experimental and computational approach designed to predict the deformation behavior of WAAM NbZr1 alloy to comprehend the PSP relationship. CP method has been successfully implemented to simulate stress-strain behavior of WAAM NbZr1 alloy incorporating distinctive microstructural characteristics. The results of the calibration and validation simulation demonstrate good agreement with the experimental observations, indicating better reliability of the model.

2. Proposed methodology

Fig. 1 shows the proposed methodology consisting of three sections: experimentation, RVE generation, and CP simulation. The following sections briefly explain the overall methodology.

The experimental part consists of the fabrication of a WAAM NbZr1 thin wall structure, microstructure characterization, and mechanical testing of the fabricated component. NbZr1 thin wall structure is fabricated using an in-house developed gas tungsten arc (GTA)-WAAM system. Microstructure characterization involves obtaining statistical information regarding grain morphology and crystallographic texture. In this study, the electron backscattered diffraction (EBSD) analysis has been performed and the dataset is used to extract information about grain size, shape, and crystal orientation. This data is required for the virtual microstructure synthesis in the subsequent steps. The tensile test has been conducted at room temperature in two orientations: one along the build direction for model calibration and another along the deposition direction for model validation. Tensile samples with different orientations have been selected to reduce bias in the simulation and improve the reliability of the model. Digital imaging correlation (DIC) is integrated into the tensile test to analyze local stress-strain behavior and explore anisotropic characteristics. Section 3 provides a detailed description of the procedures outlined above.

The first step of the simulation process is to synthesize a virtual

microstructure known as a representative volume element (RVE). It should represent the experimental microstructural features from EBSD analysis. The RVE is generated using the DREAM.3D software (v6.5.171). The software has the capability to directly incorporate experimental microstructural features and generate the RVE identical to the experimental microstructures. Grain texture and morphology data obtained from the EBSD analysis including grain size distribution, Euler angles, and aspect ratio data are directly incorporated in the software. Initially, a single large RVE is generated to incorporate significant number of grains. Smaller RVEs are subsequently extracted from the larger one to perform the simulation more efficiently. Virtual microstructure cropped along the build direction is utilized in calibration simulation and those cropped along deposition direction is used for validation simulation. The results are visualized using the ParaView software (v5.12). The attributes of virtual microstructures are validated to ensure that they contain proper repetitiveness of experimental grain statistics. This step mainly develops the linkage between experimental microstructure and RVE. The overall steps are explained in detail in

Upon the generation of RVEs, geometry and material configuration files are generated using DREAM.3D software. The geometry file mainly consists of grid points, physical size of RVE, phases, grain texture and morphology. The most important attributes of the material configuration file are definition of crystal structure, slip planes, and values of CP constitutive parameters. These files can be directly incorporated into the FFT-based DAMASK framework to run the simulation. Section 4.2 explains the theoretical background of the phenomenological CP model which is utilized in this study. CP simulations are performed in DAM-ASK, which virtually generate stress-strain curves, providing insights into the deformation behavior. The software integrates constitutive models and enables application of boundary conditions including external loading configurations, and constraints on the displacement or rotation along certain planes. The loading condition is kept consistent with the experimental tensile test. Using a trial-and-error approach, the

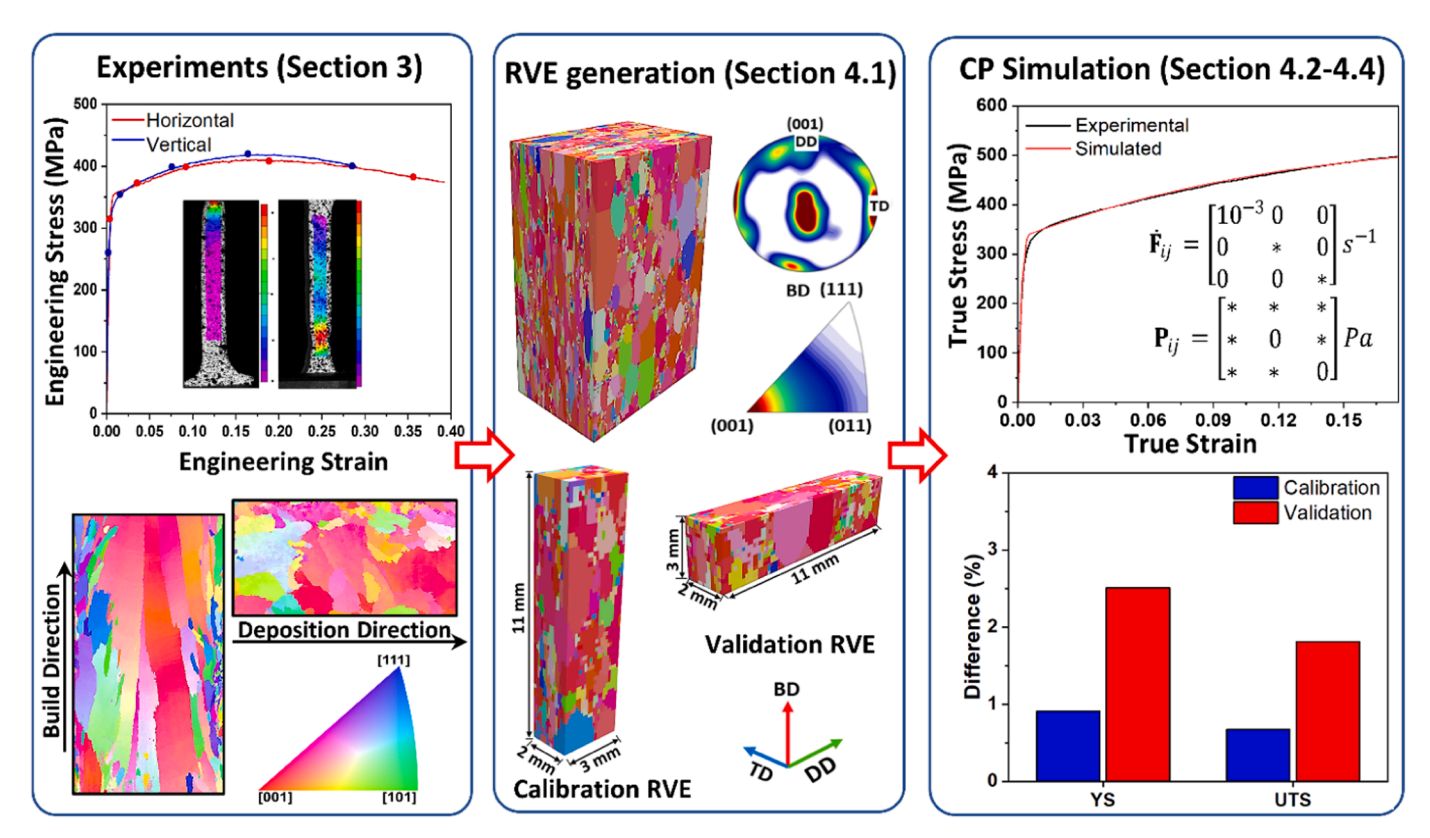


Fig. 1. Proposed methodology for the study.

constitutive parameters are calibrated until the predicted stress-strain curve matches with the experimental data. A similar approach has been implemented in the study of Bulgarevich et al. [34]. Validation of the model has been performed, utilizing these calibrated CP parameters to predict the stress-strain curve in validation RVE. Post-processing is performed afterward which involves analyzing the results of the simulation and extracting information about stress-strain curves, texture evolution, or deformation mechanisms. Simulated stress-strain curves are compared with experiments to represent the accuracy of the model. A comprehensive discussion of these procedures is provided in Sections 4.2–4.4.

3. Experimental results

3.1. Data preparation

3.1.1. Thin wall deposition

The WAAM system consists of a 6-axis Fanuc ArcMate 120iC robot arm with a Fanuc R-J3iB controller, a Miller Dynasty 400 GTA welding power source, and a wire feeder as shown in Fig. 2. The wire feeder and power source individually adjust the feed speed and welding current, respectively. A torch travel speed is modulated by the welding robot. A consistent spacing of 5 mm has been maintained between the substrate and tungsten electrode tip throughout the deposition process to ensure consistency of the voltage. Details of the experimentation have been explained in an earlier study [7]. No microstructural defects such as cracks or pores were found in the deposited structure. Previous study of the author explains in detail the forming quality of WAAM NbZr1 [7]. Tables 1 and 2

3.1.2. Sample preparation for microstructure and mechanical property analysis

The material characterization specimens have been cut at the location, as presented in Fig. 3 using the wire electrical discharge machine (EDM). After cutting, the samples are hot-mounted, grounded, and polished. The samples are also chemically polished, using a solution of 96 ml Colloidal Silica ± 2 ml Ammonium Hydroxide ± 2 ml Hydrogen Peroxide. A Helios 5 Hydra Dual Beam scanning electron microscope (SEM) integrated with an EDAX EBSD detector has been used to perform the material characterization. The data has been collected and initially analyzed using the EDAX OIM software, and post-processed using MTEX-5.9.0 extension with the MATLAB code. EDM machine has been used to generate two tensile test specimens from the deposited wall, one with a gauge section along the build direction and the other along the deposition direction as shown in Fig. 3. The gauge section of the tensile specimen is $11 \times 3.175 \times 2$ mm 3 .

At room temperature, the uniaxial tensile test has been conducted, using the TestResources 810 E4 Electrodynamic Test Machine with a strain rate of $10^{-3}~\text{s}^{-1}$. A digital image correlation (DIC) setup has been incorporated during the tensile test, as exhibited in Fig. 4. A 14.929 \times 14.929 mm² grid panel of 9 \times 9 dots and 1.78 mm pitch size is utilized for the calibration process. The subset size has been maintained at 27 \times 27 pixels and the corresponding step size is 7 pixels. The gauge section of

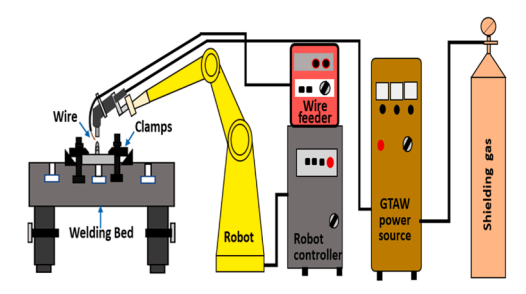


Fig. 2. Schematic diagram depicting the GTA-WAAM configuration [7].

the tensile specimens has been focused, and images are continuously captured during the tensile test until the final rupture. Images are taken at a rate of 5 Hz to match the test acquisition rate. The VIC-Snap software has been utilized to capture the images, and corresponding strain calculations are performed in VIC-3D (Correlated Solutions, Inc.) software [35]. Lagrangian and logarithmic Hencky strains have been calculated from the measured displacements. Using a 15-pixel Gaussian smoothing decay filter, the spatial and displacement resolutions are enhanced for analysis.

3.2. Microstructure analysis using EBSD

The EBSD analysis has been performed along two perpendicular planes of the specimen. This process allows for the stereological derivation of different aspects of 3D grains without the requirement of 3D EBSD experiments [18]. Multiple images are taken and merged to incorporate more grains in the analysis. BD, DD, and TD in Fig. 5 denote the build direction, deposition direction, and thickness direction, respectively. On the TD-BD plane, ten images are taken and merged with a total scanned area of $8.6 \times 5.11 \text{ mm}^2$. On the DD-TD plane, the total scanned area is $6.5 \times 3.66 \text{ mm}^2$. Fig. 5 shows the inverse pole figure (IPF) map for both regions. In Fig. 5(a), it can be found that columnar grains are formed with a major axis parallel to the BD. Layer interfaces have also been marked in the figure. The coloring of the IPF maps shows that the <001> directions of the columnar grains are aligned along the BD. This phenomenon is commonly observed and reported in other studies during the WAAM process [7]. Some of the grains have grown across multiple layers. Smaller grains could be found at the side of the IPF map. The heat transfer at the side of the walls is faster, compared to the middle due to higher convection and radiation possible with surroundings. This feature promotes finer grains towards the side of the wall. Grains along the DD-TD plane are coarse equiaxed in shape, as shown in Fig. 5(b). However, some of the equiaxed grains are very large.

In the case of AM, the pole figure data can provide insights into crystal orientation and texture formation throughout the process. To have same alignment between the grains of two perpendicular planes, rotation matrix has been applied to transform Euler angles of the TD-BD plane using MTEX-5.9.0 extension in MATLAB. Grain area fraction has been included as weight factor with the Euler angles for generating the pole figures. Fig. 6 shows the pole figure images for WAAM NbZr1 specimens. In both cases, the pronounced cluster of data points at the figure center indicates that the <001> crystal directions of the central grains are strongly aligned along the BD. The distributed intensity observed along the pole figure's outer edge suggests that some of the <001> grain orientations are aligned with DD and TD. These might be due to the presence of smaller grains at the side of the microstructure. Moreover, they constitute a small area fraction resulting in weaker texture. The center is a little bit dislocated which can be attributed to the tilt of the grains in relation to the BD as evident in the IPF map in Fig. 5. The center in Fig. 6(b) (001) is deviated from the center due to tilt as well as rotation of the sample surface during the experiments which causes the scanning to be no longer parallel to DD/TD.

Fig. 7 displays the grain size distribution for the WAAM NbZr1 specimen. The equivalent circle diameter (ECD), indicative of grain size, is equal to the circle diameter which encompasses the respective grain area [36]. In the TD-BD plane, the grain size varies significantly. Minimum grain size is 18 μm and maximum grain size is 3260 μm . Only two larger grains constitute almost 36.4% of the EBSD measurement area. Although the number of grains smaller than ECD of 50 μm is high (about 33%), their area fraction is only 1.3%. To measure the average grain size, smaller grains with ECD less than 20 μm are omitted. The average grain size has been measured 295 μm for the TD-BD plane. Similar characteristics are also observed for the grain morphology from the DD-TD plane. Moreover, compared to the TD-BD plane, the variation in grain size is smaller. Mean grain size measures 251 μm . The log-normal distribution is used to characterize the grain size distribution. The

Table 1
NbZr1 wire composition (wt%) utilized during experiments [7].

Alloying Elements	Nb	Zr	Ta	0	W	Mo	Hf	С	N	Fe	Al	Si	Ni
Composition (wt%)	Bal.	0.8-1.2	0.05	0.025	0.05	0.05	0.02	0.01	0.01	0.01	0.005	0.005	0.005

Table 2
Different parameters for the fabrication of WAAM NbZr1 thin wall [25].

Deposition Condition	Travel Speed (mm/ min)	Current (A)	Wire feed speed (mm/ min)	Energy density (J/ mm ³)	Heat input (J/mm)
1	200	200	1500	153	900

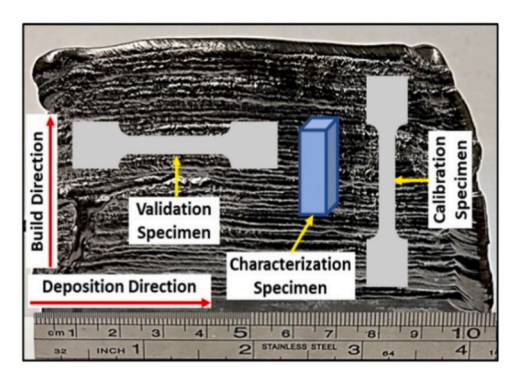


Fig. 3. Deposited NbZr1 thin wall and location of uniaxial tensile tests and microstructure characterization specimens.

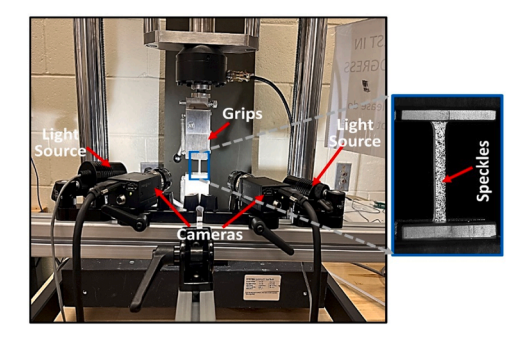


Fig. 4. Experiment setup for tensile test with DIC for WAAM NbZr1.

log-normal parameter μ and σ values for the TD-BD plane are 4.84 and 1.31, respectively. In the DD-TD plane, the μ and σ values are 4.78 and 1.13, respectively.

3.3. Mechanical property investigation

Engineering stress-strain curves of the tensile tested specimens are depicted in Fig. 8. Table 3 provides a summary of the tensile test results. The 0.2% offset initial yield strength (YS) and ultimate tensile strength (UTS) for the DD specimen are 358 MPa and 410 MPa, respectively. In BD specimens, YS and UTS have been measured to be 327 MPa and 418 MPa, respectively. YS is higher in DD specimens whereas UTS is higher in BD specimens. However, the difference is not significant. This trend might be due to plastic anisotropy, which is prevalent in the WAAM structure [37]. This feature could be explained with a true instantaneous strain-hardening exponent, n_i , which has been calculated, using the following equation:

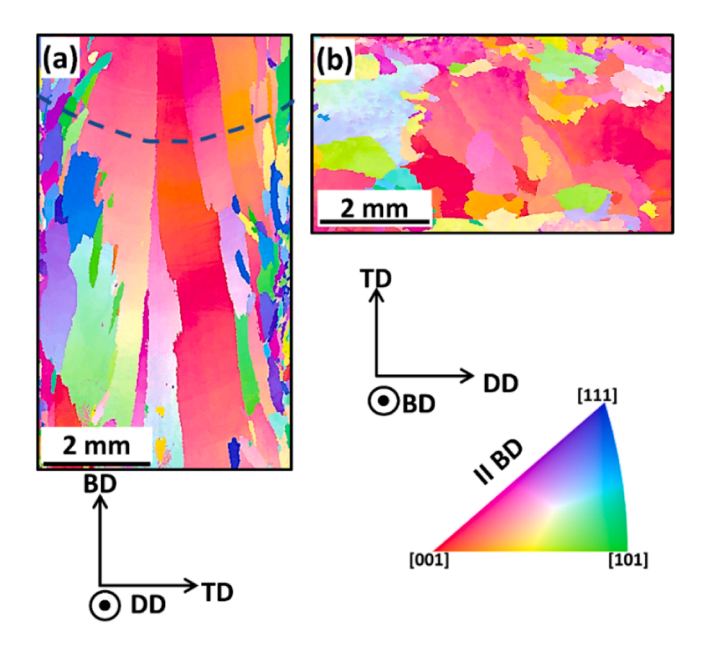


Fig. 5. Inverse pole figure map showing the grains of WAAM NbZr1 deposit: (a) TD-BD plane and (b) DD-TD plane.

$$n_i = \frac{\ln \sigma}{\ln \varepsilon} \tag{1}$$

where σ and ε are the true stress-strain. It is shown in Fig. 8(b), n_i is larger for the BD specimens, which contributes to the higher UTS. Similar findings have been also described in the study of Kindermann et al. [37]. The uniform elongation limits for DD and BD specimens are 19.4% and 17.3%, respectively. The corresponding total elongations are 37.5% and 27.1%. Higher elongation indicates that both samples showed good ductility during the test. Nevertheless, DD specimens showed better ductility compared to BD. BD specimen consists of a multiple-layer interface and interlayer region [7]. Due to the segregation of elements in these regions, the mechanical strength varies within the tensile sample. It can cause strain concentration, premature failure, and reduced ductility. In contrast, in horizontal specimens, layer differences uniformly influence the entire specimen length, without distinct sections of varying strength [38]. Similar results have been reported in other studies [38,39]. The true UTS values for the DD and BD specimens at corresponding uniform elongations of 19.4% and 17.3% are 486 MPa and 496 MPa, respectively. Young's modulus has been measured to be 102 GPa and 117 GPa for the DD and BD specimens, respectively, revealing significant anisotropy in elastic stiffness contributed to the alignment of <001> crystal orientations along the BD. Young's modulus also has been calculated using the Euler angles. The corresponding values are 107 GPa and 113 GPa in the DD and BD.

4. Crystal plasticity simulation results

4.1. Representative Volume Element (RVE) generation

First step of the CP simulation is RVE generation. It is one of the most important aspects of the CP simulation. The RVE should contain all the necessary information to be representative of the original

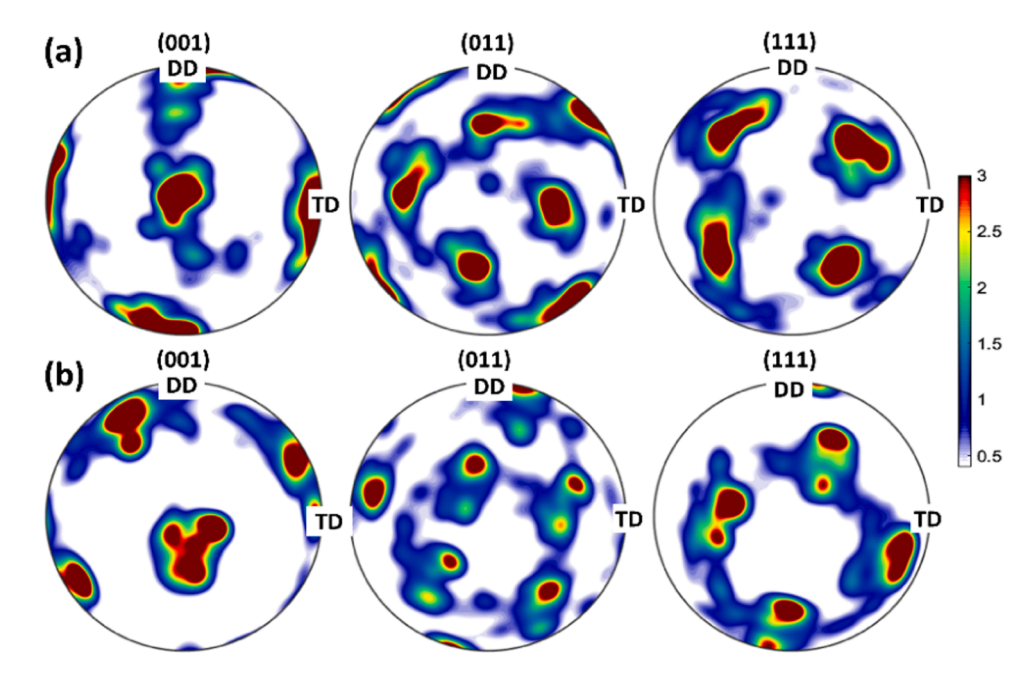


Fig. 6. Pole figure showing the crystal orientation of WAAM NbZr1 deposit: (a) TD-BD plane and (b) DD-TD plane.

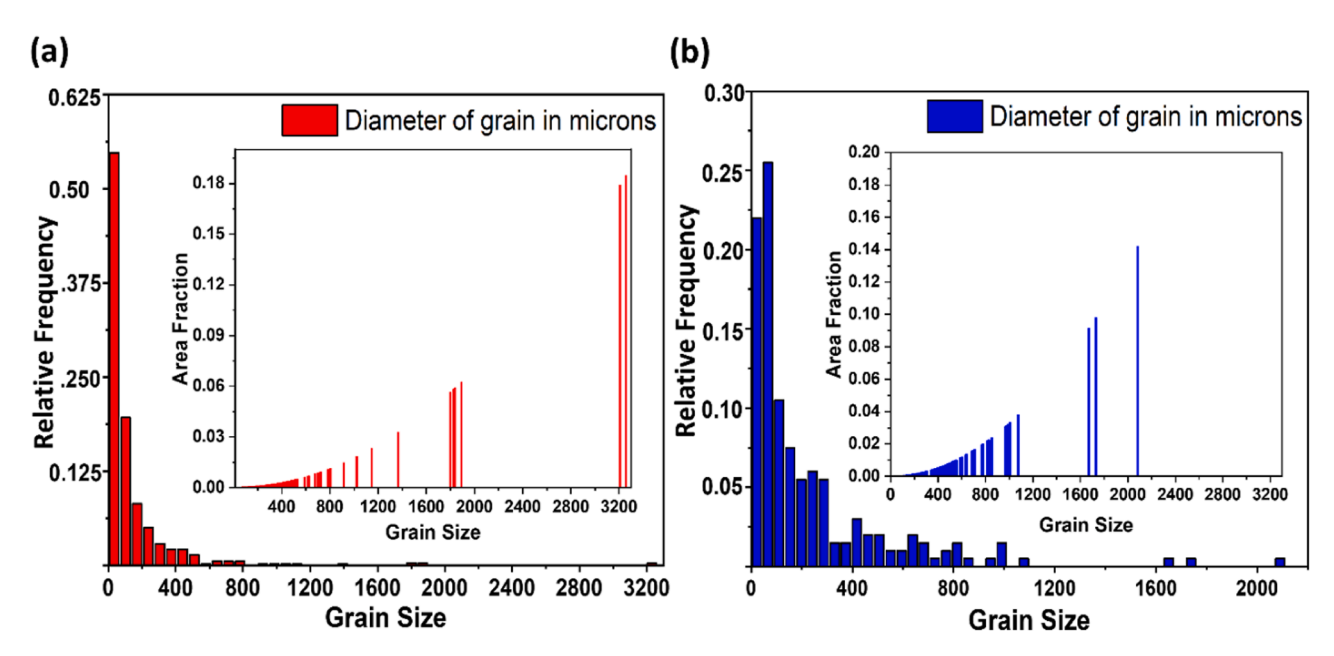


Fig. 7. Grain Size distribution map for WAAM NbZr1 specimen: (a) TD-BD plane and (b) DD-TD plane.

microstructure. Based on the grain morphology and the texture data characterized from the EBSD analysis in Section 3.2, a 3D RVE has been generated, using the DREAM.3D software [17]. The pipeline used in generating the RVE is shown in the Appendix. The statistical microstructure information obtained from the EBSD analysis is assigned in the 'StatsGenerator' filter in DREAM.3D using the single-phase BCC crystal structure. Details of each filter can be found in the software database.

The DREAM.3D software generates synthetic 3D microstructures by modeling grains as ellipsoids. It is required to estimate the three axes of the ellipsoidal grains by utilizing grain size distribution from EBSD analysis. ECD, which is measured utilizing EBSD in the TD-BD plane is considered as the principal axis (largest) of the ellipsoid as shown in Fig. 9. ECD measured from the EBSD data in the DD-TD plane is the equivalent axis of the ellipsoid in the normal direction. The other axis is calculated using the experimental grain aspect ratio data. Fig. 9 presents

the schematic diagram showing an ellipsoid and its principal axes as well as two corresponding EBSD planes. After deriving all three axes of individual grain, ellipsoidal volume is calculated and consequently, equivalent sphere diameter (ESD) is derived for individual grain. ESD is equivalent to the ellipsoidal grain size. ESD value is directly incorporated in the 'StatsGenerator' filter of DREAM.3D software. The Euler angles obtained from EBSD analysis along two orthogonal planes are directly integrated into the 'StatsGenerator' filter to assign crystal orientation to the grains. In addition, the area fraction of each grain is incorporated as a weight factor within the Euler angle file to incorporate the effect of grain size on the texture. The average grain aspect ratio acquired from both the TD-BD and DD-TD planes is directly implemented in the software as shown in Fig. 9.

From the experimental data, it has been found that grains parallel to the BD are very coarse spanning multiple layers. It is very difficult to

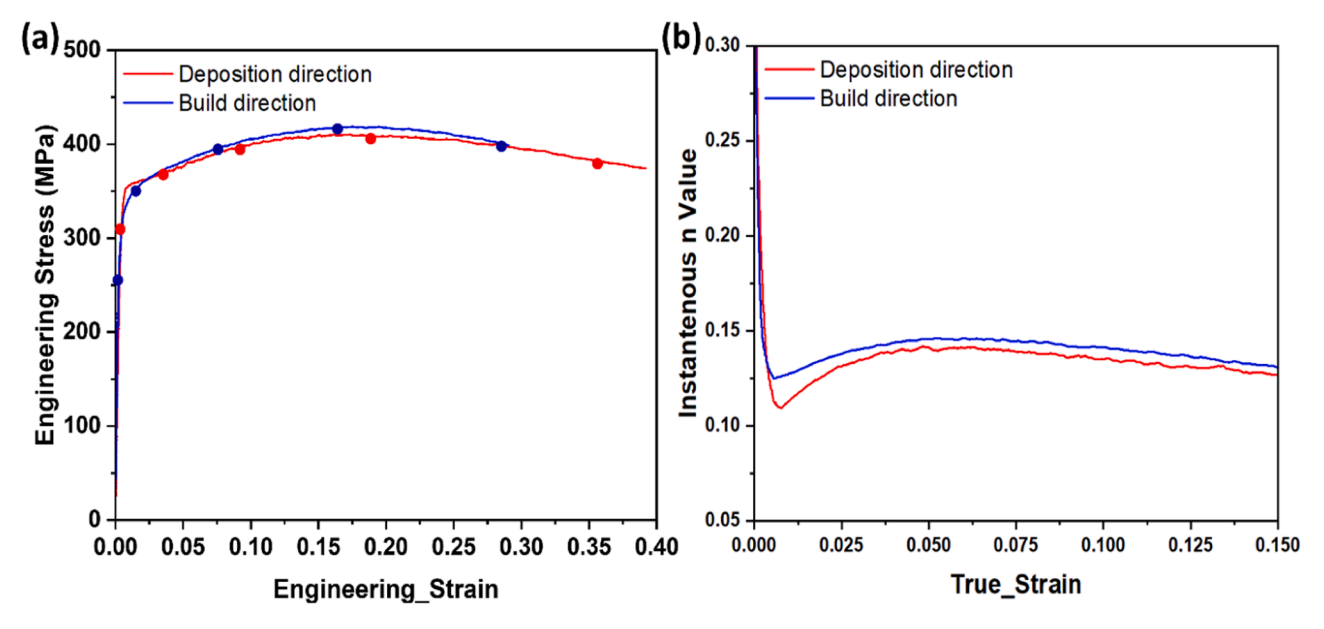


Fig. 8. (a) Engineering stress-strain curves and (b) corresponding instantaneous strain hardening exponents for WAAM NbZr1 tensile specimens.

Table 3Tensile test data summary for the WAAM NbZr1 specimen.

Orientation	YS (MPa)	UTS (MPa)	Uniform Elongation (%)	Total Elongation (%)	Young's Modulus (GPa)
Deposition direction	358	410	19.4	37.5	102
Build direction	327	418	17.3	27.1	117

incorporate a significant number of grains in the RVE if the size is small. On the contrary, larger RVE is computationally inefficient to run the simulation. To encounter this trend, one larger RVE is generated, using the DREAM.3D software to incorporate all the microstructural features. Fig. 10 shows the generated RVE. It consists of $128\times128\times128$ voxels with a resolution of $200\times150\times100$ along the x, y, and z directions. The specified voxel size is $1\times1\times1~\mu\text{m}^3$. The total dimension of the big RVE is $25.6\times19.2\times12.8~\text{mm}^3$, which contains more than 80,000 grains.

From the large RVE, smaller microstructures parallel to BD and DD,

characterized as calibration and validation RVEs are cropped to run the simulation. Fig. 11 shows the generated calibration and validation RVE. This step is to evaluate the effect of relatively large grains located inside the gauge volume of tensile samples on the overall mechanical behavior. The crop RVE consists of $55\times20\times20$ voxels with a resolution of $200\times150\times100$ along the x, y, and z directions. The specified voxel size is the same as the big RVE. The cropped RVE size is $11\times3\times2$ mm 3 , close to the dimension of the actual tensile specimen gauge volume and contains more than 1000 grains in each condition. It is evident from the morphology and texture of the calibration RVE that elongated grains are formed parallel to the BD, which resembles the experimental microstructure.

In Fig. 12, the attributes of 3D RVE generated with DREAM.3D are compared with experimental microstructure to validate their statistical equivalence and accuracy. Fig. 12 shows the comparison of the grain morphology and texture between the simulated RVEs and the merged experimental grain information from the TD-BD and DD-TD planes. The pole and inverse pole figures match closely with data from the experiments, as presented in Fig. 12(a) and (b). In both instances, the major texture is parallel to the BD. To compare the grain morphology, both the

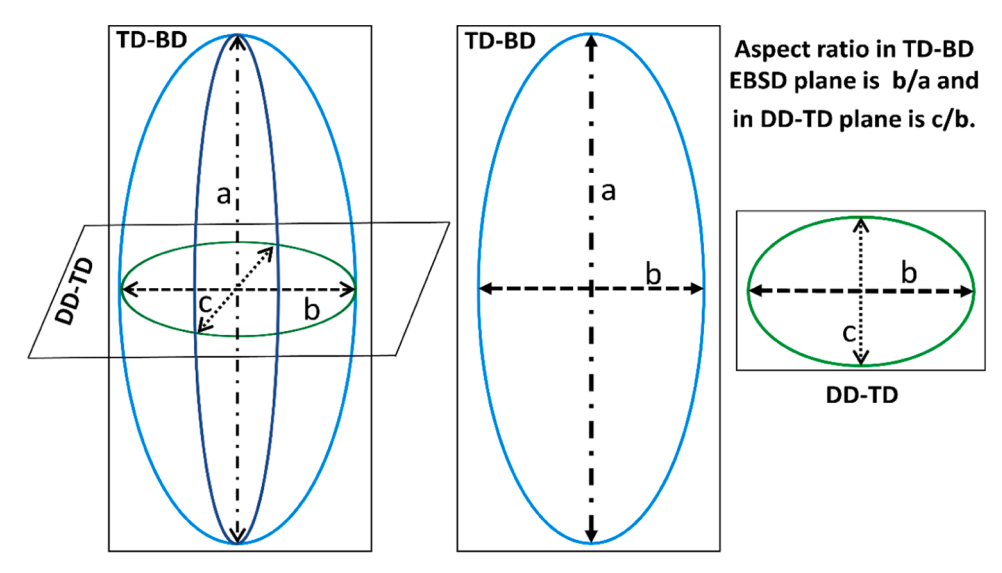


Fig. 9. Schematic diagram showing ellipsoid and two EBSD planes.

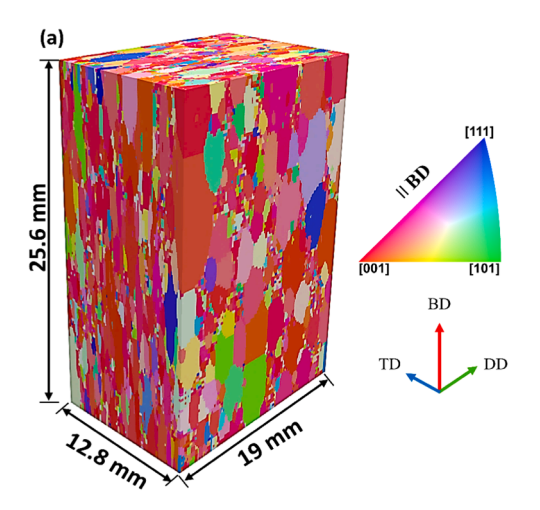


Fig. 10. Generated 3D RVE for WAAM NbZr1 using DREAM.3D.

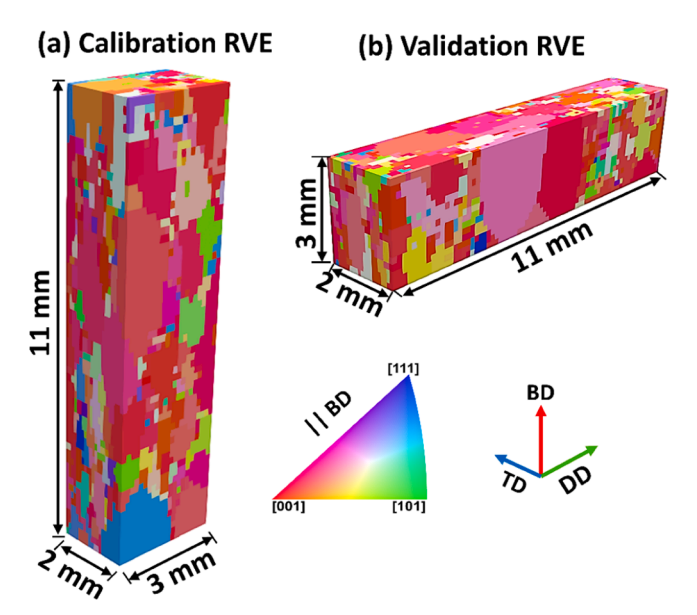


Fig. 11. Cropped RVE from Generated 3D RVE of WAAM NbZr1: (a) calibration RVE and (b) validation RVE.

aspect ratio and grain size distributions have been considered. The aspect ratio is fitted with the beta distribution function, and the lognormal distribution function has been used to fit the grain morphology. The average grain ESD calculated from experiments is 281 μ m. The calculated ESD for the RVE is 292 μ m, as shown in Fig. 12 (c). The mean aspect ratios along the BD and DD are 0.35 and 0.41, respectively, for the experimental data. For the simulated RVE, these values are 0.35 and 0.46, respectively, as shown in Fig. 12(d). Overall, the grain statistics of the simulated 3D virtual microstructure and experimental data are well aligned when compared. It can be concluded that the simulated RVE captures all the necessary microstructural information required to be considered a representative RVE. In the literature, it has been explained that [40], if the RVE size is 50 times more than the average grain size, the differences in predicted properties will be less than 1%. In our case, the cropped RVEs are approximately 40 times the average grain size, indicating that RVE is size representative enough to provide good accuracy and repeatability.

4.2. Crystal plasticity framework

After generating the RVE, the next step is to perform the simulation.

The DAMASK spectral solver [41] has been utilized in this study to perform CP simulations. The FFT is an efficient method for solving the CP boundary value problem, especially with large RVEs that contain complex microstructural features [41]. Furthermore, the linking of DREAM.3D with DAMASK can be performed by introducing the filter, 'Export DAMASK Files,' in the RVE generation pipeline. This filter enables direct export of the resulting RVE to a geometry file that can be processed by FFT applications. The CP model utilized in this study is an adaptation of the modified phenomenological model outlined for BCC crystals [42] within the DAMASK framework [43]. According to the model, plastic deformation is assumed to occur on a slip system when the resolved shear stress surpasses a critical threshold [42,43].

Given the assumption that plastic deformation occurs due to the dislocation slip, the plastic velocity-gradient tensor, \mathbf{L}_p , is given by,

$$\mathbf{L}_p = \sum_{\alpha=1}^{24} \dot{\gamma}^{\alpha} \mathbf{b}^{\alpha} \otimes \mathbf{n}^{\alpha}$$

Here, \mathbf{b}^{α} and \mathbf{n}^{α} refer to unit vectors that characterize the slip direction and the normal direction to the slip plane within the α -th slip system, respectively. $\dot{\gamma}^{\alpha}$ denotes the slip rate of the slip system. The kinetic law governing the activation of each slip system is described as follows:

$$\dot{\gamma}^{\alpha} = \dot{\gamma}_0 \left| \frac{ au^{lpha}}{S^{lpha}} \right|^n ext{sgn} \ (au^{lpha})$$

where, $\dot{\gamma}_0$ is the reference slip rate, and n is the stress exponent. The resolved shear stress, $\tau^{\alpha} = \mathbf{\sigma} \cdot (\mathbf{b}^{\alpha} \otimes \mathbf{n}^{\alpha} + \mathbf{n}^{\alpha} \otimes \mathbf{b}^{\alpha})/2$, is obtained by the stress, $\mathbf{\sigma}$, while S^{α} is the critical resolved shear stress.

Slip resistance, S^{α} , on 12 {011} <111> and 12 {211} <111> slip systems are indexed by $\alpha=1, 2, ...24$. These slip resistances increase with the applied $\dot{\gamma}^{\alpha}$ up to S^{α}_{∞} as described by the following relationship:

$$\dot{S}^{lpha} = \sum_{lpha=1}^{24} h_0 ig(1 - S^{lpha} ig/ S_{\infty}^{lpha}ig)^a h_{lphaeta} \dot{\gamma}^{lpha},$$

where h_0 , a, and S_{∞} are hardening parameters. $h_{\alpha\beta}$ denotes the diagonal and off-diagonal components of the interaction matrix.

4.3. CPFFT model calibration

The CP model has been calibrated by matching the simulated stress-strain data with the BD tensile test specimen. The major axis for the calibration RVE is along the x-direction, which is parallel to the BD. The current work incorporated mixed boundary conditions uniaxially along the RVE's x-direction. It is ensured that the out-of-plane surfaces in all geometries remain free of stress, and a strain rate of $1\times 10^{-3}~\text{s}^{-1}$ has been maintained to precisely mimic the conditions of tensile experiments.

where, $\dot{\mathbf{F}}_{ij}$ is the deformation gradient rate, and \mathbf{P}_{ij} is the first Piola-Kirchhoff stress tensor. Components marked with an asterisk (*) are assigned complementary conditions.

The focus of the calibration model is to match the simulated curve exactly with the experimental curve by optimizing different constitutive parameters. The elastic constants used in the simulation are C_{11} , C_{12} , and C_{44} with the value of 228 GPa, 124 GPa, and 27 GPa, respectively [44,45]. The shear-strain rate and stress exponent, n, do not significantly affect the plastic region of the stress-strain curve. The exponent, n, has

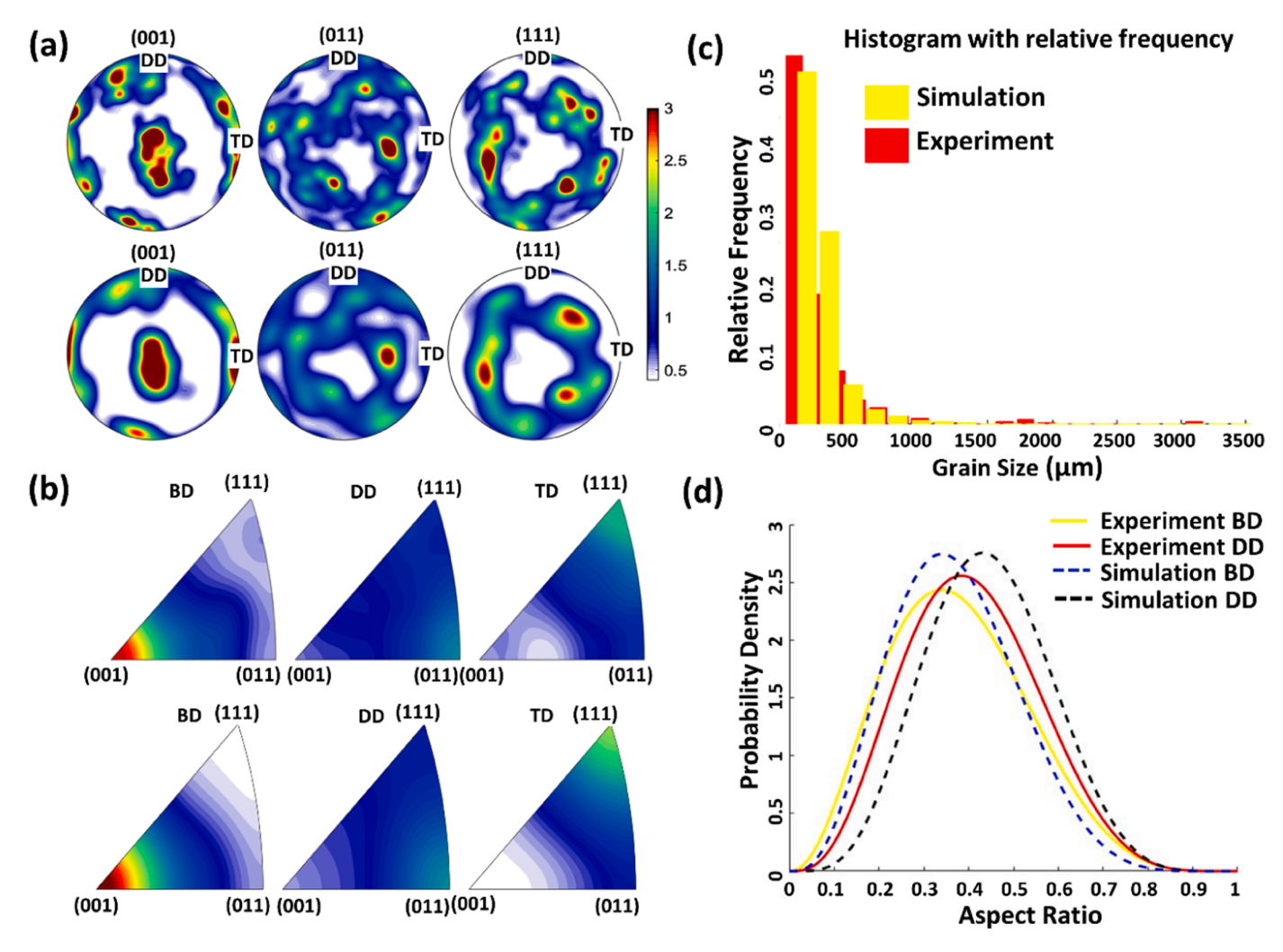


Fig. 12. Comparison of grain morphology and texture between experimental EBSD data and simulated RVE: (a) pole figure, (b) inverse pole figure, (c) grain size distribution, and (d) aspect ratio in WAAM NbZr1.

no physical meaning and is usually used as a numerical variable to approximate the Schmidt law. The value of these parameters is kept constant during the simulation and has been collected from the literature as $1\times 10^{-3}~{\rm s}^{-1}$ and 20 [43]. $h_{\alpha\beta}$ denotes the interaction-hardening parameters. The components of $h_{\alpha\beta}$ are distinguished into diagonal ($\alpha=\beta$) and off-diagonal ($\alpha\neq\beta$), representing self and latent hardening, respectively. For self-hardening, the value has been used as 1.0 and for latent hardening as 1.4 [46]. The constant CP parameters throughout the simulation are outlined in Table 4.

An iterative approach has been implemented to calibrate the model, adjusting its parameters until the simulation result precisely matches the experimental data. For calibration of the plastic region, true stress-strain data has been employed. The four iteratively varied parameters are initial slip resistance, S_0 , saturation slip resistance S_∞ , slip hardening parameter, h_0 , and curve-fitting parameter, h_0 . Among them, the

Table 4Constant CP parameters for the simulation.

Symbol	Attributes	Unit	
C ₁₁	228	GPa	
C ₁₂	124	GPa	
C ₄₄	27	GPa	
$\dot{\gamma}_0$	1×10^{-3}	s^{-1}	
$h_{lphaeta}$	1.0, 1.4	-	
n	20	-	

parameter, a, is utilized to indirectly account for the effect of interactions between slip systems. The influence of various CP parameters on the stress-strain curve has been included in the Appendix. The calibrated constitutive parameters are summarized in Table 5.

Fig. 13 compares the predicted result from the calibrated CPFFT model with the experimental result. The simulation was performed up to a 0.173 true strain. It can be found that the calibrated CP-model curves and experimental curves match closely with each other. The YS and true UTS for the calibrated model are 330 MPa and 492 MPa, respectively. The difference values with the experiment are 0.91% and 0.67%, measured using Eq. (2). As the difference is lower than 1.0%, it can be concluded that the CP constitutive parameters have been calibrated successfully.

Difference(%) =
$$\left| \frac{p^{\text{Model}} - p^{\text{Experiment}}}{p^{\text{Experiment}}} \right| \times 100$$
 (2)

Table 5Calibrated phenomenological constitutive model parameters for the simulation.

Parameter Definition	Symbol	Attributes	Unit
Initial slip resistance on {011} <111>	S_0	166	MPa
Saturation slip resistance on {011} <111>	S_{∞}	379	MPa
Initial slip resistance on {211} <111>	S_0	167	MPa
Saturation slip resistance on {211} <111>	S_{∞}	389	MPa
Slip hardening parameter	h_0	1100	MPa
Curve fitting parameter	а	2.0	-

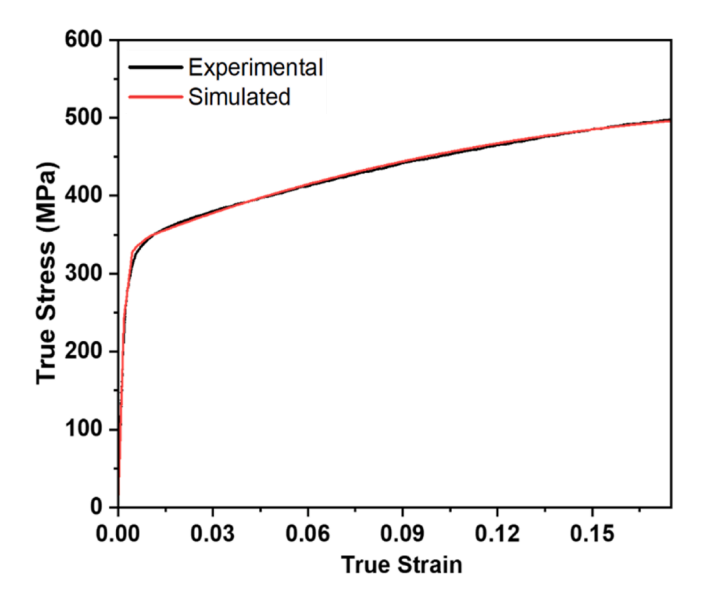


Fig. 13. Comparison between the optimized calibration simulation and experimental tensile results along the BD.

4.4. Model validation

For the model validation, RVE along the DD, which has not been utilized for the calibration, is considered, and the load is applied along the y-direction, which mimics the experimental tensile test condition along the DD. The loading condition is described as follows:

$$\dot{\mathbf{F}}_{ij} = \begin{bmatrix} \& * \&\&0\&\&0\\ \&0\&1\&\&0\\ \&0\&\&0\&\&* \end{bmatrix} \times 10^{-3} \cdot s^{-1}$$

The simulation is performed up to 19.4% of the true strain. The calibrated parameters summarized in Table 5 have been used for the validation simulation. The simulated validation curve matches closely to

the experimental one, as shown in Fig. 14. YS and UTS for the validation simulation are 349 MPa and 495 MPa respectively. To evaluate the model precision more comprehensively, YS and UTS are derived from the stress-strain curves and then compared using Eq. (2). The difference in YS is 2.51% and UTS is 1.81% respectively. Table 6 summarizes the difference between calibration and validation simulation results with the experimental ones.

5. Discussion

The CP parameters have been calibrated by running the simulation using cropped RVE along the BD. The microstructure and boundary conditions are different for the validation simulation in which RVE is cropped along the DD. Since different RVE and loading conditions provide a close match between the experimental and predicted curves, it can be concluded that the CP model is validated [30]. In this study, the difference in YS and UTS is 2.51% and 1.81% respectively, indicating high accuracy. Similar accuracy has also been reported in other studies. In the study of Park et al. [22], it has been found that the average error percentage is 2.25% for normalized yield stress. Azhari et al. [30] found that the maximum error between the experimental stress-strain curve and that obtained from the CP-FE simulation is around 2% in most regions of the stress-strain curve in their study. They concluded that incorporating appropriate microstructural characteristics into the RVE from experimental data leads to improved accuracy of the model. Fig. 12 shows that experimental and simulated RVE characteristics match closely which has contributed to higher accuracy in this model.

From Fig. 8, which illustrates the average stress-strain behavior, *YS* along the BD is lower, compared to the DD. Whereas *UTS* is higher in the DD relative to the BD. It represents evidence of anisotropy in the deposited structure, which is similar to the findings of the previous study [7]. The use of a single physical strain gauge cannot provide accurate results if heterogeneity is present in the microstructure. In addition, the

Table 6The difference between model prediction and experimental results.

RVE	YS (%)	UTS (%)
Calibration	0.91	0.67
Validation	2.51	1.81

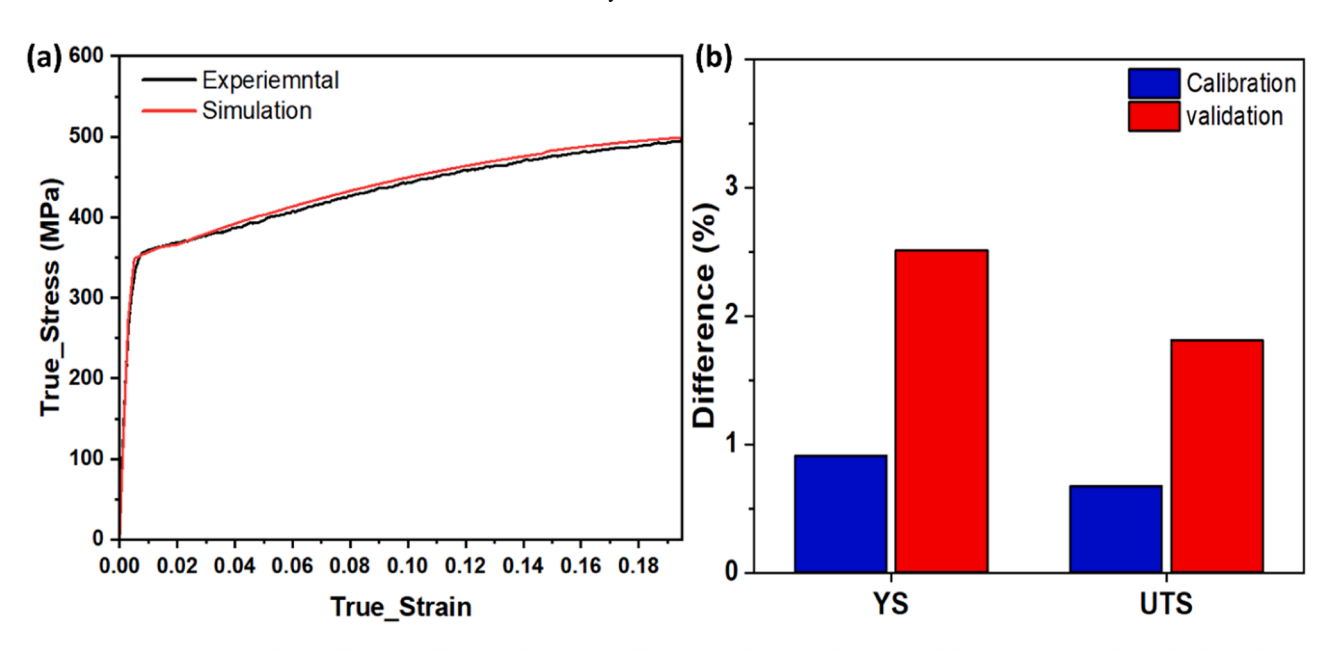


Fig. 14. (a) Comparison between the validation simulation and experimental tensile results along the DD, (b) differences in YS and UTS for the calibration and validation simulation.

global strain of the stress-strain curve is the average of the entire gauge section, making it impossible to interpret the location-specific deformation behavior. Therefore, the DIC analysis has been performed in this study to analyze local deformation behavior because of their unique microstructure, compared to traditional materials [47]. Fig. 15 describes the DIC analysis results for WAAM NbZr1 specimens. A scale bar is shown in each figure to identify a local strain distribution. Fig. 15(a) shows the analysis of the BD specimen. The leftmost figure presents the region of analysis before the application of an external load. Different locations in the stress-stain curves identified in Fig. 8 have been denoted as P1-P5 based on the increasing strain values. In the elastic region, the strain field is uniform, although little strain is found due to the bucking of the sample. This trend may be due to the residual stress in the samples. As the applied load increases, the sample starts to deform plastically, as shown in P2. With further elongation, local stress concentration occurs at the top of the sample. With the increase in load, necking occurs, and the load-bearing capacity starts to decrease. When the local strain reaches a maximum value, the sample fails. The strain evolution of the BD specimen is similar to conventional materials. Fig. 15(b) shows the analysis for the DD specimen. In the elastic region, the strain distribution is uniform. With the increase of the applied load, strain localization occurs at the middle region of the specimen. As the strain increases, strain localization shifts to the bottom of the specimen. Necking also occurs at that location, and the specimen fails accordingly. The result indicates the presence of heterogeneity due to the relatively large size of central grains, compared to the dimensions of the tensile specimen, as exhibited in Fig. 5.

The simulated stress-strain curves in the calibration and validation cases match very closely with the experimental ones. In the calibration simulation, the difference in *YS* and *UTS* is within 1.0%. In full-field simulations, the global stress-strain is the average response of material behavior and does not provide information regarding the local stress-strain concentration. In the WAAM case, as explained in the DIC analysis local stress-strain might be different while having the same global

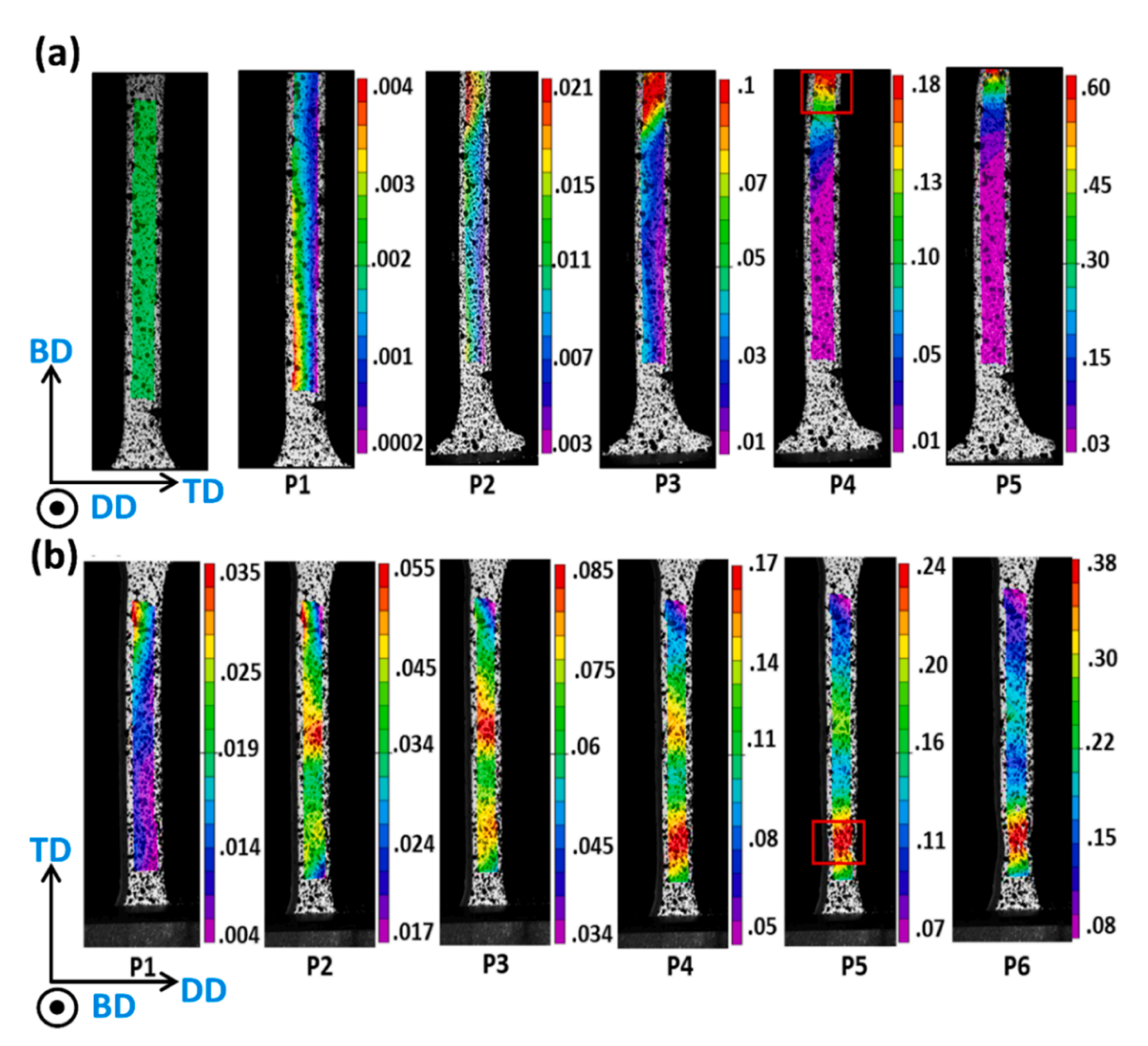


Fig. 15. Strain evolution during the tensile test of WAAM NbZr1 deposit: (a) BD specimen and (b) DD specimen.

deformation. To analyze these results computationally, three different RVEs are cropped from the larger one to study the global and local stress-stain behavior. The principal axis of the grains is parallel to the BD. Simulation results are summarized in Fig. 16. The global deformation behavior shown in Fig. 16(a) indicates that the stress-strain curves match very closely with each other. Visually from the local stress-strain distribution in Fig. 16(b) and (c), the von Mises stress-strain looks different. The location of stress concentration varies with respect to different RVEs. Although the same scale has been used to show the stress variation within the RVEs, it is difficult to visually differentiate between the results. To statistically compare the results, the probability density function (PDF) has been calculated and shown in Fig. 16(d) up to a strain of 35%. The result reveals that there has been a clear difference in the local stress-strain behavior among the RVEs, indicating anisotropy.

To study the RVE size sensitivity on the simulation results, three different RVEs are generated, using the DREAM.3D software having dimensions of $32 \times 32 \times 32$, $64 \times 64 \times 64$, and $128 \times 128 \times 128$ with a resolution of $10 \times 10 \times 10$ along the three directions, following the procure explained in Section 5.2. The calibrated CP parameters summarized in Table 5 have been used for the simulation. Load is applied parallel to columnar grains, similar to the BD condition up to a strain of 20%. Uniaxial tension simulation results are summarized in Fig. 17. It can be found that stress-strain curves match closely in each of the simulation cases. There has been an exceedingly small variation in the UTS with a difference of values of less than 1.0%, which is negligible. It can be concluded that, if the grain statistics remain the same, the RVE size does not considerably affect the stress-strain behavior.

6. Conclusions

This paper provides a methodology for generating RVE and predicting mechanical properties for wire-arc additively manufactured NbZr1 components. Full-filed CPFFT simulations on the DAMASK platform have been performed to predict the stress-strain property as well as global and local deformation behavior.

- The EBSD analysis from two perpendicular planes has been incorporated in generating the RVEs to consider the effect of grain size and crystal orientation. The statistical microstructure characteristics obtained from the simulated RVEs match closely with the experimental measurements.
- The model calibration has been performed by adjusting the CP parameters to match the simulated stress-strain curves in the BD with the experimental data using trial and error methods. Variation in YS and UTS of less than 1.0% indicates a good match between the predicted and experimental curves.
- The calibrated CP parameters have been utilized for the validation of uniaxial tension simulations in the DD. The validation result shows good agreement with the experimental data having a difference of YS and UTS within 2.51% and 1.81% respectively.
- The presence of anisotropy in the microstructure, as evidenced by the DIC analysis and CPFFT simulation, highlights the complex nature of material behavior at the microstructural level. Understanding and characterizing this anisotropic behavior is crucial for predicting and optimizing the mechanical properties of materials in various engineering applications.

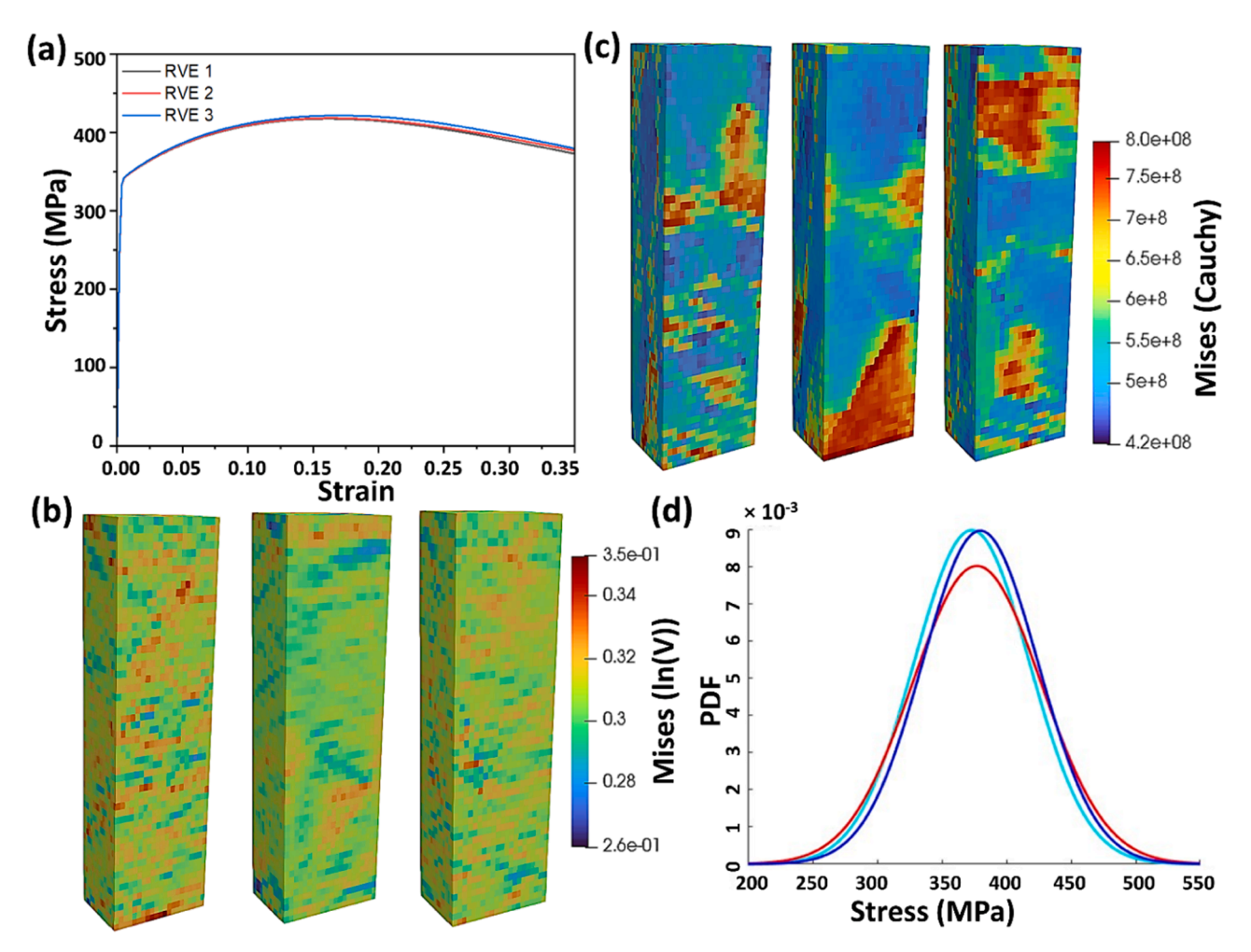


Fig. 16. (a) stress-strain curves, (b) strain distribution, (c) von Mises stress distribution (Pa), and (d) PDF for stress analysis for three different RVEs.

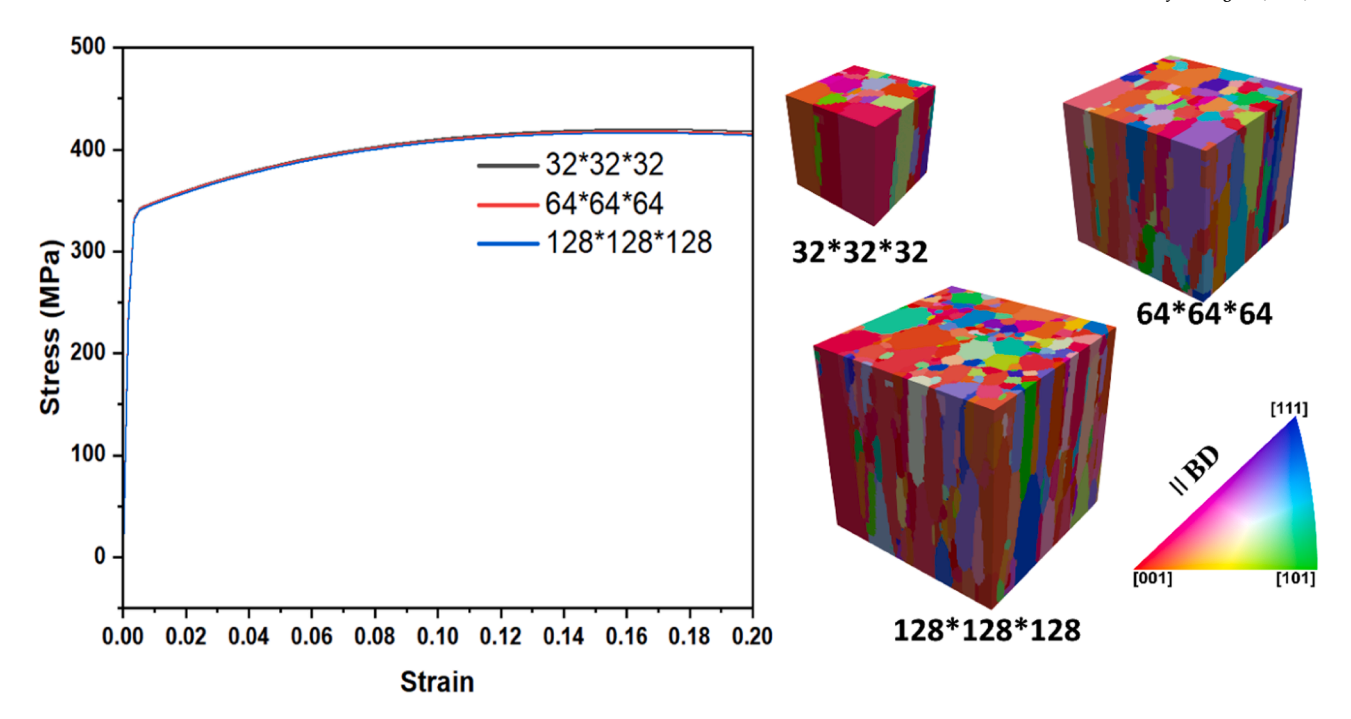


Fig. 17. RVE size sensitivity analysis for WAAM NbZr1.

Although the result indicates good agreement, still there are some mismatches between the experimental and simulation results. This trend might be due to the inability of the CPFFT model developed in this study to account for the distribution of residual stresses arising from uneven thermal strain in the WAAM process. Unlike the surface of actual specimens that distorts depending on the grain morphology during uniaxial tension tests, the use of periodic boundary conditions in the CPFFT model forces to maintain a smooth and parallel surface, potentially influencing the strain-localization behavior. For a more accurate representation of the microstructure characteristics, detailed sub-grain scale features, such as the dendritic structure formation and sub-grain boundaries, need to be incorporated into the RVE. However, these are out of the scope of the present study. The authors plan to expand this study and implement these concerns in future research. The approach explained in the study, which combines computational and experimental methods, can be utilized for other refractory alloys to predict mechanical properties, and advance the fundamental understanding of the PSP relationship.

CRediT authorship contribution statement

Duck Bong Kim: Conceptualization, Funding acquisition, Investigation, Methodology, Project administration, Resources, Supervision, Writing – review & editing. **Peter K. Liaw:** Conceptualization, Resources, Writing – review & editing. **Sainand Jadhav:** Writing – review

& editing, Investigation, Data curation. **Saiful Islam:** Writing – original draft, Validation, Methodology, Investigation, Formal analysis, Conceptualization. **Farhang Pourboghrat:** Writing – review & editing, Methodology, Conceptualization. **Taejoon Park:** Writing – review & editing, Methodology, Investigation, Conceptualization. **Xuesong Fan:** Writing – review & editing, Resources, Data curation.

Declaration of Competing Interest

The authors declare that they have no known competing financial interests or personal relationships that could have appeared to influence the work reported in this paper.

Data availability

Data will be made available on request.

Acknowledgements

The authors of this paper acknowledge the Center for Manufacturing Research (CMR) and Tennessee Technological University's Department of Manufacturing and Engineering Technology for their support. This material is based upon work supported by the National Science Foundation under Grant No. 2141905.

Appendix

Figure A1 shows the pipeline used in the DREAM.3D software for the generation of RVEs.



Figure A1. DREAM.3D pipeline for generating the RVE.

The parameter sensitivity analysis is performed to identify the impact of each parameter on the overall tensile stress-strain curve. The result is summarized in Figure A2. Figure A2(a) shows the effect on the initial slip resistance. S_0 has a direct effect on yield strength. With the increase of S_0 , yield strength increases. The effect of S_∞ has been summarized in Figure A2(b). With the increase of S_∞ , the yield strength increases a little while the strain hardening increases significantly with the increase of UTS. The macro-strain hardening rate also depends on the slip hardening parameter, S_0 0, Although the yield strength remains the same, with the increase of S_0 1, strain hardening increases. Figure A2(d) shows that the strain hardening rate decreases with the increase of a value.

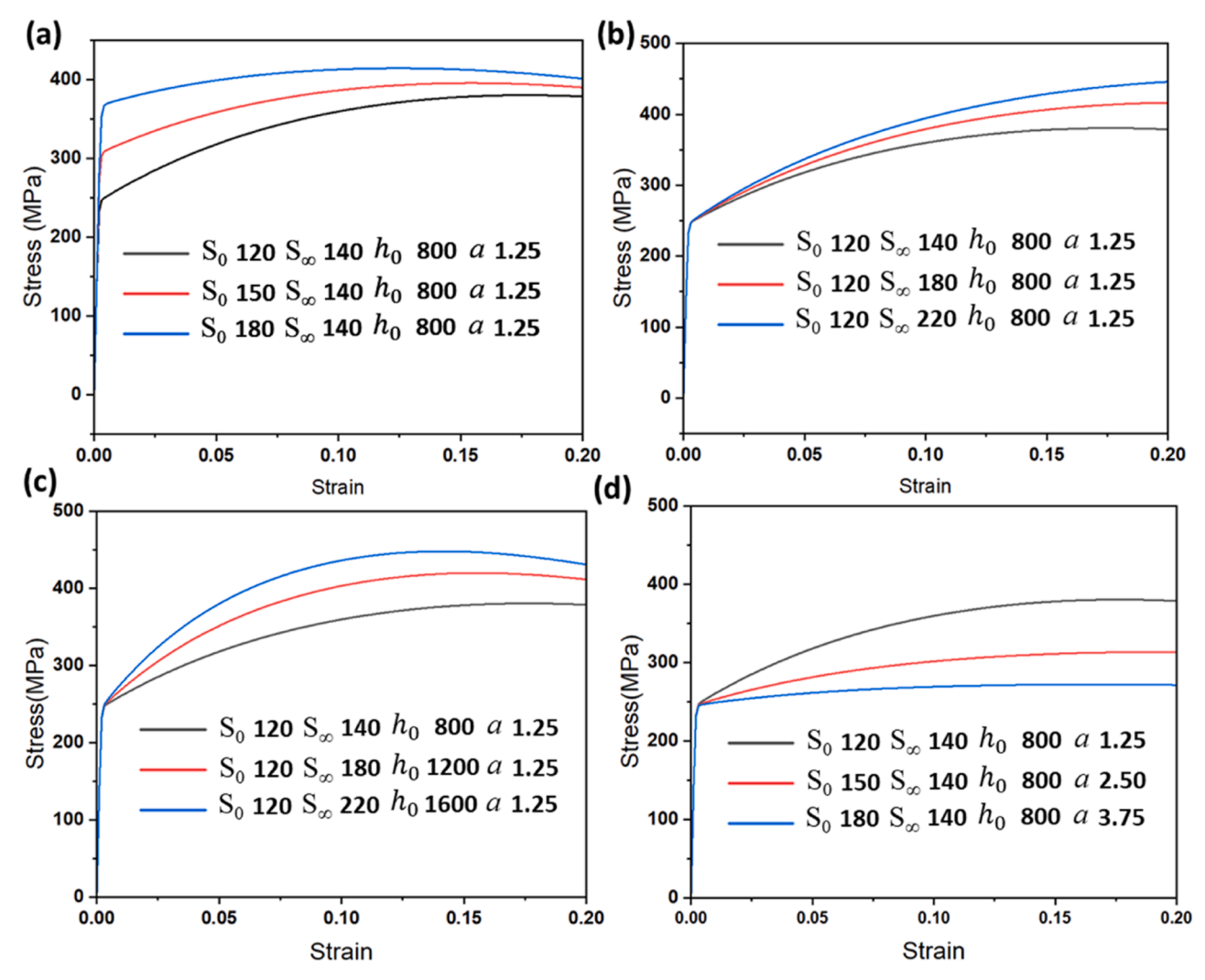


Figure A2. Effect of calibration parameter on the overall stress-strain behavior.

References

- [1] P.D. Awasthi, P. Agrawal, R.S. Haridas, R.S. Mishra, M.T. Stawovy, S. Ohm, A. Imandoust, Mechanical properties and microstructural characteristics of additively manufactured C103 niobium alloy, Mater. Sci. Eng. A vol. 831 (2022) 142183. https://doi.org/10.1016/j.msea.2021.142183.
- [2] S. Islam, G.-J. Seo, M.R.U. Ahsan, H. Villarraga-Gómez, H.-J. Lee, D.B. Kim, Investigation of microstructures, defects, and mechanical properties of titaniumzirconium-molybdenum alloy manufactured by wire arc additive manufacturing, Int. J. Refract. Met. Hard Mater. vol. 110 (2023) 106042, https://doi.org/10.1016/ j.ijrmhm.2022.106042.
- [3] F. Pixner, R. Buzolin, F. Warchomicka, A. Pilz, N. Enzinger, Wire-based electron beam additive manufacturing of tungsten, Int. J. Refract. Met. Hard Mater. vol. 108 (2022) 105917, https://doi.org/10.1016/j.ijrmhm.2022.105917.
- [4] L. Gardner, Metal additive manufacturing in structural engineering review, advances, opportunities and outlook, Structures vol. 47 (2023) 2178–2193, https://doi.org/10.1016/j.istruc.2022.12.039.
- [5] A. Vafadar, F. Guzzomi, A. Rassau, K. Hayward, Advances in metal additive manufacturing: A review of common processes, industrial applications, and current challenges, Appl. Sci. vol. 11 (3) (2021) 1–33, https://doi.org/10.3390/ APP11031213.
- [6] H. Yi, L. Jia, J. Ding, H. Li, Achieving material diversity in wire arc additive manufacturing: Leaping from alloys to composites via wire innovation, Int. J. Mach. Tools Manuf. vol. 194 (2024) 104103, https://doi.org/10.1016/j. ijmachtools.2023.104103.
- [7] S. Islam, M.R.U. Ahsan, G.J. Seo, H.J. Lee, T. Park, F. Pourboghrat, D.B. Kim, Investigations of Microstructure and Mechanical Properties in Wire + Arc Additively Manufactured Niobium-Zirconium Alloy, Adv. Eng. Mater. vol. 25 (15) (2023) 2201633, https://doi.org/10.1002/ADEM.202201633.

- [8] G. Robert Odette, S.J. Zinkle, Structural alloys for nuclear energy applications, Struct. Alloy. Nucl. Energy Appl. (2019) 1–655, https://doi.org/10.1016/C2011-0-07772-4.
- [9] Q. Ding, H. Bei, X. Zhao, Y. Gao, Z. Zhang, Processing, microstructures and mechanical properties of a Ni-based single crystal superalloy, Crystals vol. 10 (7) (2020) 1–14. https://doi.org/10.3390/cryst10070572.
- [10] A. Sarkar, R. Kapoor, A. Verma, J.K. Chakravartty, A.K. Suri, Hot deformation behavior of Nb-1Zr-0.1C alloy in the temperature range 700-1700 °c, J. Nucl. Mater. vol. 422 (1–3) (2012) 1–7, https://doi.org/10.1016/j. inurnat 2011 11 064
- [11] S.K. Gupta, S. Jaypuria, D.K. Pratihar, P. Saha, Experimental investigation on microstructure and mechanical properties of laser-welded Nb-1% Zr-0.1% C alloy, J. Mater. Eng. Perform. 2021 3011 vol. 30 (11) (2021) 8412–8425, https://doi. org/10.1007/S11665-021-05979-8.
- [12] T.A. Rodrigues, V. Duarte, R.M. Miranda, T.G. Santos, J.P. Oliveira, Current status and perspectives on wire and arc additive manufacturing (WAAM), Mater. (Basel) vol. 12 (07) (2019), https://doi.org/10.3390/ma12071121.
- [13] B. Wu, Z. Pan, D. Ding, D. Cuiuri, H. Li, J. Xu, J. Norrish, A review of the wire arc additive manufacturing of metals: properties, defects and quality improvement, J. Manuf. Process. vol. 35 (2018) 127–139, https://doi.org/10.1016/j. jmapro.2018.08.001.
- [14] J. Xiong, C. Wen, Arc plasma, droplet, and forming behaviors in bypass wire arcdirected energy deposition, Addit. Manuf. vol. 70 (2023) 103558, 10.1016/j. addma.2023. 103558.
- [15] S.M. Hashemi, S. Parvizi, H. Baghbanijavid, A.T.L. Tan, M. Nematollahi, A. Ramazani, N.X. Fang, M. Elahinia, Computational modelling of process-structure-property-performance relationships in metal additive manufacturing: a review, Int. Mater. Rev. vol. 67 (1) (2022) 1–46, https://doi.org/ 10.1080/09506608.2020.1868889.

- [16] T.M. Rodgers, H. Lim, J.A. Brown, Three-Dimensional Additively Manufactured Microstructures and Their Mechanical Properties, JOM vol. 72 (1) (2020) 75–82, https://doi.org/10.1007/s11837-019-03808-x.
- [17] X.X. Zhang, H. Andrä, Crystal plasticity simulation of the macroscale and microscale stress-strain relations of additively manufactured AlSi10Mg alloy, Comput. Mater. Sci. vol. 200 (2021) 110832, https://doi.org/10.1016/J. COMMATSCI.2021.110832.
- [18] J. Galán-López, J. Hidalgo, Use of the Correlation between Grain Size and Crystallographic Orientation in Crystal Plasticity Simulations: Application to AISI 420 Stainless Steel, Crystals vol. 10 (9) (2020) 819, https://doi.org/10.3390/ cryst10090819.
- [19] W. Li, L. Wang, B. Zhou, C. Liu, X. Zeng, Grain-scale deformation in a Mg-0.8 wt% Y alloy using crystal plasticity finite element method, J. Mater. Sci. Technol. vol. 35 (10) (2019) 2200-2206, https://doi.org/10.1016/j.jmst.2019.04.030.
- [20] G.Y. Deng, C. Lu, L.H. Su, X.H. Liu, A.K. Tieu, Modeling texture evolution during ECAP of copper single crystal by crystal plasticity FEM, Mater. Sci. Eng. A vol. 534 (2012) 68–74, https://doi.org/10.1016/J.MSEA.2011.11.042.
- [21] M. Uchida, K. Tsutsumi, M. Sakamoto, Y. Kaneko, Characterization of size-affected non-uniform deformation of polycrystalline copper, Int. J. Mech. Sci. vol. 211 (August) (2021) 106760, https://doi.org/10.1016/j.ijmecsci.2021.106760.
- [22] T. Park, H. Lim, B. Reedlunn, S. Kramer, E. Corona, F. Pourboghrat, The impact of heterogeneous microstructural features on crystal plasticity modeling of plastic anisotropy, Model. Simul. Mater. Sci. Eng. vol. 29 (7) (2021) 075004, https://doi. org/10.1088/1361-651X/ac1ce9.
- [23] M. Diehl, M. Groeber, C. Haase, D.A. Molodov, F. Roters, D. Raabe, Identifying Structure-Property Relationships Through DREAM.3D Representative Volume Elements and DAMASK Crystal Plasticity Simulations: An Integrated Computational Materials Engineering Approach, JOM vol. 69 (5) (2017) 848–855, https://doi.org/10.1007/s11837-017-2303-0.
- [24] M. Umar, F. Qayyum, M.U. Farooq, L.A. Khan, S. Guk, U. Prahl, Analyzing the cementite particle size and distribution in heterogeneous microstructure of C45EC steel using crystal plasticity based DAMASK code, *Proc. 18th* (Jan), Int. Bhurban Conf. Appl. Sci. Technol. IBCAST 2021 (2021) 15–20, https://doi.org/10.1109/IBCAST51254.2021.9393292.
- [25] H. Lim, J.D. Carroll, C.C. Battaile, B.L. Boyce, C.R. Weinberger, Quantitative comparison between experimental measurements and CP-FEM predictions of plastic deformation in a tantalum oligocrystal, Int. J. Mech. Sci. vol. 92 (2015) 98–108. https://doi.org/10.1016/j.ijmecsci.2014.12.010.
- [26] L.T. Hansen, D.T. Fullwood, E.R. Homer, R.H. Wagoner, H. Lim, J.D. Carroll, G. Zhou, H.J. Bong, An investigation of geometrically necessary dislocations and back stress in large grained tantalum via EBSD and CPFEM, Mater. Sci. Eng. A vol. 772 (2020) 075015, https://doi.org/10.1016/j.msea.2019.138704.
- [27] C. Wang, Z.J. Li, C.Q. Ji, S.W. Gao, Y.N. Cui, Crystal plasticity analysis of the evolutions of temperature, stress and dislocation in additively manufactured tungsten, Int. J. Refract. Met. Hard Mater. vol. 110 (Nov) (2023), https://doi.org/ 10.1016/j.jimphm.2022.106041.
- [28] X. Xiao, D. Terentyev, A. Ruiz, A. Zinovev, A. Bakaev, E.E. Zhurkin, High temperature nano-indentation of tungsten: Modelling and experimental validation, Mater. Sci. Eng. A vol. 743 (October 2018) (2019) 106–113, https://doi.org/ 10.1016/j.msea.2018.11.079
- [29] D.H. Ahn, G.G. Lee, J. Moon, H.S. Kim, Y.B. Chun, Analysis of texture and grain shape effects on the yield anisotropy of Zr-2.5wt%Nb pressure tube alloy using crystal plasticity finite element method, J. Nucl. Mater. vol. 555 (2021) 153112, https://doi.org/10.1016/j.inucmat.2021.153112.
- [30] F. Azhari, C. Wallbrink, Z. Sterjovski, B.R. Crawford, A. Menzel, D. Agius, C. H. Wang, G. Schaffer, Predicting the complete tensile properties of additively manufactured Ti-6Al-4V by integrating three-dimensional microstructure statistics with a crystal plasticity model, Int. J. Plast. vol. 148 (2022) 103127, https://doi.org/10.1016/j.ijplas.2021.103127.
- [31] A. Chakrabarty, R. Chakraborty, R. Jain, V.K. Sahu, N.P. Gurao, H.N. Bar, N. Khutia, Influence of scanning and building strategies on the deformation behavior of additively manufactured AISi10Mg: CPFEM and finite element studies, Met. Mater. Int. vol. 29 (2023) 2978–3008, https://doi.org/10.1007/s12540-023-01418-6.

- [32] S.A.H. Motaman, F. Roters, C. Haase, Anisotropic polycrystal plasticity due to microstructural heterogeneity: A multi-scale experimental and numerical study on additively manufactured metallic materials (Feb), Acta Mater., Vol. 185 (2020) 340–369, https://doi.org/10.1016/j.actamat.2019.12.003.
- [33] S.S. Acar, O. Bulut, T. Yalçinkaya, Crystal plasticity modeling of additively manufactured metallic microstructures, Procedia Struct. Integr. vol. 35 (2021) 219–227, https://doi.org/10.1016/j.prostr.2021.12.068.
- [34] D.S. Bulgarevich, S. Nomoto, M. Watanabe, M. Demura, Crystal plasticity simulations with representative volume element of as-build laser powder bed fusion materials, Sci. Rep. vol. 13 (2023) 20372, https://doi.org/10.1038/s41598-023-47651-2
- [35] A. Lescur, E. Stergar, J. Lim, S. Hertelé, R.H. Petrov, Investigation of the Dynamic Strain Aging Effect in Austenitic Weld Metals by 3D-DIC, Met. (Basel) vol. 13 (2) (2023), https://doi.org/10.3390/met13020311.
- [36] W. Liu, J. Lian, N. Aravas, S. Münstermann, A strategy for synthetic microstructure generation and crystal plasticity parameter calibration of fine-grain-structured dual-phase steel, Int. J. Plast. vol. 126 (2020) 102614, https://doi.org/10.1016/J. LIPLAS.2019.10.002.
- [37] R.M. Kindermann, M.J. Roy, R. Morana, J.A. Francis, Effects of microstructural heterogeneity and structural defects on the mechanical behaviour of wire + arc additively manufactured Inconel 718 components, Mater. Sci. Eng. A vol. 839 (2022) 142826, https://doi.org/10.1016/j.msea.2022.142826.
- [38] G. Mirone, R. Barbagallo, S. Di Bella, Effect of process parameters on the mechanical properties of a Titanium alloy fabricated by Electron Beam Melting (EBM), IOP Conf. Ser. Mater. Sci. Eng. vol. 1214 (2022) 012001 org/10.1088/ 1757-899x/1214/1/012001.
- [39] L. Sun, F. Jiang, R. Huang, D. Yuan, C. Guo, dJ. Wang, Anisotropic mechanical properties and deformation behavior of low-carbon high-strength steel component fabricated by wire and arc additive manufacturing, Mater. Sci. Eng. A. vol. 787 (2020) 139514 org/10.1016/J.MSEA.2020.139514.
- [40] K. Teferra, L. Graham-Brady, A random field-based method to estimate convergence of apparent properties in computational homogenization, Comput. Methods Appl. Mech. Eng. vol. 330 (2018) 253–270, org/10.1016/j. cma.2017.10.027.
- [41] F. Roters, P. Eisenlohr, C. Kords, D.D. Tjahjanto, M. Diehl, D. Raabe, DAMASK: The dusseldorf advanced material simulation kit for studying crystal plasticity using an fe based or a spectral numerical solver, Procedia IUTAM vol. 3 (2012) 3–10, https://doi.org/10.1016/j.pjutam.2012.03.001.
- [42] John Woodside Hutchinson, Bounds and self-consistent estimates for creep of polycrystalline materials, Proc. R. Soc. Lond. A. Math. Phys. Sci. vol. 1652 (1976) 101–127
- [43] F. Roters, M. Diehl, P. Shanthraj, P. Eisenlohr, C. Reuber, S.L. Wong, D. Rabbe, DAMASK – The Düsseldorf Advanced Material Simulation Kit for modeling multiphysics crystal plasticity, thermal, and damage phenomena from the single crystal up to the component scale, Comput. Mater. Sci. vol. 158 (2019) 420–478, https:// doi.org/10.1016/j.commatsci.2018.04.030.
- [44] X. Wang, L.B. Liu, M.F. Wang, X. Shi, G.X. Huang, L.G. Zhang, Computational modeling of elastic constants as a function of temperature and composition in Zr-Nb alloys, Calphad vol. 48 (2015) 89–94, https://doi.org/10.1016/j. calphad.2014.11.003.
- [45] B.L. Rodríguez-Espinoza, F.A. García-Pastor, B. Martínez-Poveda, A.R. Quesada, P. Lopez-Crespo, High-strength low-modulus biocompatible Nb-12r alloy processed by accumulative roll bonding, Mater. Sci. Eng. A vol. 797 (2020) 140226, https://doi.org/10.1016/j.msea.2020.140226 (Please complete the publication information (e.g., issue/page/article numbers)).
- [46] R.J. Asaro, A. Needleman, Overview no. 42 Texture development and strain hardening in rate dependent polycrystals, Acta Met. vol. 33 (6) (1985) 923–953, https://doi.org/10.1016/0001-6160(85)90188-9.
- [47] P. Kyvelou, H. Slack, D. Daskalaki Mountanou, M.A. Wadee, T.Ben Britton, C. Buchanan, L. Gardner, Mechanical and microstructural testing of wire and arc additively manufactured sheet material, Mater. Des. vol. 192 (2020) 108675, https://doi.org/10.1016/J.MATDES.2020.108675.